REVISION 2

Ab initio investigation of majorite and pyrope garnets: Lattice dynamics and vibrational spectra

MARCO DE LA PIERRE[1,*] AND DONATO BELMONTE[2]

[1] *Nanochemistry Research Institute, Curtin Institute for Computation, Department of Chemistry, Curtin University, GPO Box U1987, Perth WA 6845, Australia*

[2] *DISTAV, Università di Genova, Corso Europa 26, 16132 Genova, Italy*

ABSTRACT

A detailed ab initio quantum-mechanical characterization is presented of the vibrational properties of pyrope and majorite garnets, using the hybrid B3LYP functional and large all electron Gaussian type basis sets. Discussed quantities include infrared (both TO and LO) and Raman frequencies, normal modes coordinates, spectroscopic intensities, mode Grüneisen parameters, isotopic substitution, and infrared and Raman spectra. Comparison with data available in the literature demonstrates the accuracy of the adopted method. Main spectral features of the two garnets are interpreted in terms of either symmetry analysis or structural contributions to the vibrational modes. Missing peaks in the experiments are discussed in light of the simulated spectra. The present high quality vibrational data can be used to compute thermal expansivities at high pressure and high temperature conditions. Calculated values for majorite at the bottom of the mantle transition zone ($\alpha_V = 2.2\times10^{-5}$ K^{-1} at T = 1500 K and P = 20 GPa) turn out to be sensibly greater (up to three times) than those currently adopted in geophysical thermodynamic databases, thus calling for a careful revision of the numerical models for thermo-chemical convection of the Earth's mantle.

Keywords Infrared spectrum, Raman spectrum, vibrational frequencies, mode Grüneisen parameters, thermal expansivity, *ab initio* quantum mechanical calculations, CRYSTAL code

* Email: *marco.delapierre@curtin.edu.au*

INTRODUCTION

Thermodynamic properties of high pressure mineral phases in the system MgO-Al_2O_3-SiO_2 are crucial to understand chemico-physical processes in the Earth's mantle and to constrain the mineralogical constitution of its deeper parts. Among these phases, $MgSiO_3$ majorite garnet and its solid solutions with pyrope ($Mg_3Al_2Si_3O_{12}$) are of relevant interest as they are major components of the mantle transition zone, ranging in volume from 40% to 70% according to different petrological models (Bass and Anderson 1984; Ringwood 1991; Vacher et al. 1998; Weidner and Wang 1998; Akaogi et al. 2002). Furthermore, majorite-pyrope garnets undergo phase transitions at high pressure and temperature conditions, which may be at the origin of multiple seismic discontinuities between 520 km and 720 km depths (Hirose et al. 2001; Hirose 2002; Deuss et al. 2006; Saikia et al. 2008).

Vibrational spectroscopy, in both its infrared and Raman variants, is an invaluable tool to gather lattice dynamics data that can be used for thermodynamical modelling. Also, Raman barometry techniques are emerging as a tool in the study of mineral inclusions in diamond (e.g. Izraeli et al. 1999), of which majoritic garnets are common examples (cf. Harte 2010). In fact, these methods have been shown to provide reliable estimates of the residual internal pressure exerted by the host diamond on the inclusion, hence of their pressure of formation by the so called elastic relaxation method (Nestola et al. 2011, 2012; Angel et al. 2014). These reasons make very desirable the availability of accurate spectroscopic characterisations of the majorite-pyrope system, both at ambient and high pressure conditions.

Experimental characterization of the vibrational properties of majorite-pyrope garnets is challenging, mainly due to problems affecting their high pressure synthesis in the laboratory. Pervasive merohedral or pseudomerohedral twinning is always present in the tetragonal end-member of the majorite-pyrope series ($Mg_4Si_4O_{12}$ or, for simplicity, $MgSiO_3$), as revealed by TEM studies (Angel et al. 1989; Hatch and Ghose 1989; Wang et al. 1993). The finding of single crystals

for structural refinement is thus hindered, and IR and Raman spectra currently available for this phase could be obtained exclusively on polycrystalline samples (Kato and Kumazawa 1985; McMillan et al. 1989; Rauch et al. 1996; Manghnani et al. 1998; Chopelas 1999). Additional complications in the interpretation of the vibrational spectra arise from lowering of symmetry with respect to cubic garnets (*Ia-3d* to $I4_1/a$ space group) and from possible structural disorder.

Ab initio simulation has proved to be an excellent method to provide accurate descriptions of the vibrational properties of silicate minerals, especially when exploiting hybrid density functionals (Zicovich-Wilson et al. 2004, 2008; Prencipe et al. 2004; Pascale et al. 2005a, 2005b; Orlando et al. 2006; Valenzano et al. 2009, 2010; Ferrari et al. 2009; Dovesi et al. 2009, 2011; De La Pierre et al. 2011; Demichelis et al. 2012; Noël et al. 2012; Ulian et al. 2013; Maschio et al. 2013a, 2014; Prencipe et al. 2014; Belmonte et al. 2014; Erba et al. 2015). Contrary to the experiment, it permits to easily investigate "ideal" systems, free from the issues brought by polycrystallinity, defects, impurities, disorder. Whereas several studies are available on the vibrational spectra of pyrope (e.g. Zicovich et al. 2008; Dovesi et al. 2011; Maschio et al. 2013a; and references therein), only two recent articles can be found, exploring the vibrational properties of majorite, by Yu et al. (2011) and Hernández et al. (2015), using pure DFT (Density Functional Theory) functionals; both of them are focused on the thermodynamic properties of the minerals, so that vibrational spectra (and related accuracy issues) are discussed to a little extent.

In the present work, *ab initio* quantum mechanical calculations have been performed at an hybrid Hartree-Fock/DFT level of theory, to get new insights into the vibrational properties and the ensuing thermodynamics of majorite-pyrope end-member compositions.

The paper is organised as follows. The next Section describes the adopted computational framework. Section on Results and Discussion deals with the main aspects regarding structural properties, vibrational frequencies, infrared and Raman spectra, and additional issues like isotopic substitution and mode Grüneisen parameters. The main perspectives of this work are outlined in the Implications Section. Additional material is available on the web site in the form of Supplementary

Information.

COMPUTATIONAL METHOD

Calculations were performed with the CRYSTAL14 periodic *ab initio* code (Dovesi et al. 2014a, 2014b), by using all electron Gaussian type basis sets and the hybrid B3LYP functional (Becke 1993; Lee et al. 1988; Stephens et al. 1994).

Magnesium, aluminum, silicon and oxygen were described by (8s)-(511sp)-(1d), (8s)-(611sp)-(1d), (8s)-(831sp)-(1d) and (8s)-(411sp)-(1d) contractions, respectively. The exponents (in $bohr^{-2}$) of the most diffuse functions are $\alpha_{sp} = 0.225$ and $\alpha_d = 0.50$ for Mg, $\alpha_{sp} = 0.380$ and $\alpha_d = 0.50$ for Al, $\alpha_{sp} = 0.193$ and $\alpha_d = 0.61$ for Si and $\alpha_{sp} = 0.181$ and $\alpha_d = 0.60$ for O. These basis functions were already used in previous works on Mg-Al silicates and oxides (Ottonello et al. 2009; Ottonello et al. 2010a, 2010b; Dovesi et al. 2011; Demichelis et al. 2012; Belmonte et al. 2013, 2014; Erba et al. 2014).

The level of accuracy in evaluating the Coulomb and Hartree-Fock exchange series is controlled by five parameters (Dovesi et al. 2014a), for which the 8 8 8 9 18 values were used. The threshold on the SCF energy was set to 10^{-8} Hartree (E_h) for geometry optimisation and to 10^{-10} E_h for calculation of vibrational frequencies. The reciprocal space was sampled according to a sublattice with shrinking factor (Dovesi et al. 2014a) set to 3 (along the 3 lattice vectors), corresponding to 4 (pyrope) and 6 (majorite) independent $\vec{k}$ vectors in the irreducible part of the Brillouin zone.

The DFT exchange-correlation contribution is evaluated by numerical integration over the unit cell volume. In CRYSTAL, radial and angular points of the grid are generated through Gauss-Legendre radial quadrature and Lebedev two-dimensional angular point distributions. A (75,974)p grid was used, corresponding to a pruned grid with 75 radial and 974 angular points (XLGRID keyword in the CRYSTAL manual; Dovesi et al. 2014a). Accuracy in the integration can be estimated by the error Δe on the integrated electronic charge density in the unit cell ($\Delta e = 2 \cdot 10^{-4}$ |e|

and $3 \cdot 10^{-6}$ |e| for pyrope and majorite, respectively, on a total of 800 electrons).

Structure were optimised by using analytical energy gradients with respect to atomic coordinates and unit cell parameters (Doll 2001; Doll et al. 2001; Civalleri et al. 2001), within a quasi-Newton scheme combined with the BFGS algorithm for Hessian updating (Broyden 1970; Fletcher 1970; Goldfarb 1970; Shanno 1970). Convergence was checked on both gradient components and nuclear displacements, for which the default values (Dovesi et al. 2014a) were chosen.

The calculation of vibrational frequencies at the Γ point ($\nu_{0,n}$) was performed within the harmonic approximation; the mass-weighted Hessian matrix W is constructed by numerical differentiation of the analytical gradients with respect to the atomic Cartesian coordinates:

$$W_{\alpha i,\beta j}(\Gamma) = \frac{H_{\alpha i,\beta j}}{\sqrt{M_\alpha M_\beta}} \quad (1)$$

where $H_{\alpha i,\beta j}$ is the second derivative of energy (evaluated numerically starting from the analytical gradients), M_α and M_β are the atomic masses; greek and latin indices refer to atoms and atomic Cartesian coordinates, respectively. The calculated (optimised) equilibrium geometry is taken as reference. More details on the calculation of vibrational frequencies can be found in Pascale et al. (2004), Zicovich-Wilson et al. (2004) and Zicovich-Wilson et al. (2008).

Once the Hessian matrix H is calculated, frequency shifts due to isotopic substitutions can be obtained at zero computational cost, by changing the masses in Equation (1). This possibility was exploited to evaluate the participation of the various atoms to the vibrational modes in the different regions of the spectrum. In particular, the masses of Mg, Al, Si and O were augmented by 7.5% in separate runs.

Infrared absorption intensities II_n were computed for each n-th mode by means of the mass-weighted effective mode Born charge vector (Barrow 1962; Hess et al. 1986), evaluated through a Berry phase approach (Dall'Olio et al. 1997; Baranek et al. 2001; Noël et al. 2002); see Zicovich-Wilson et al. (2008) for more details. Isotropic Raman intensities II_n were computed for each mode

through a fully analytical, coupled perturbed Hartree-Fock/Kohn-Sham scheme (Maschio et al. 2013b, 2013c).

A graphical representation of the infrared and Raman spectra $S(\nu)$ was obtained as a superposition of Lorentzian functions F, one for each mode:

$$S(\nu) = \sum_n F(\nu; \nu_{0,n}, II_n, \delta_n) \quad (2)$$

$$F(\nu; \nu_{0,n}, II_n, \delta_n) = \frac{II_n}{\pi}\left[\frac{\delta_n/2}{(\nu-\nu_{0,n})^2 + \delta_n^2/4}\right] \quad (3)$$

where δ_n is the damping factor of the n-th mode, which is related to the phonon lifetime. Being unable to compute this quantity, we used a constant value of 8 cm^{-1}. S(ν) curves were evaluated in the range 0-1100 cm^{-1}, in steps of 1 cm^{-1}.

Mode Grüneisen parameters (γ_n) define the volume dependence of the vibrational frequencies in the framework of quasi-harmonic approximation (QHA) as follows:

$$\gamma_n = -\left(\frac{\partial \ln \nu_{0,n}}{\partial \ln V}\right)_0 = -\frac{V}{\nu_{0,n}}\left(\frac{\partial \nu_{0,n}}{\partial V}\right)_0 \quad (4)$$

where V is the unit cell volume. Values for these quantities were obtained by least-square fitting of the vibrational frequencies computed at four different volume conditions (V/V_0 = 0.88, 0.99, 1.00 and 1.01 for majorite; V/V_0 = 0.80, 0.90, 0.95 and 1.00 for pyrope). For each mineral the three frequency datasets close to the uncompressed volume condition (i.e. V/V_0 = 1) permit an accurate mapping of the frequency behaviour close to the minimum of the potential energy surface. Besides, the additional dataset at high compression accounts for the high pressure conditions. Second-order polynomial fitting turns out to accurately describe the volume dependence of all the vibrational frequencies.

Calculated and experimental frequencies ν_i were compared through three global indices defined as follows:

$$\overline{|\Delta|} = M^{-1}\sum_{i=1}^{M}\left|\nu_i^{calc} - \nu_i^{exp}\right| \quad (5)$$

$$\bar{\Delta} = M^{-1}\sum_{i=1}^{M}\left(\nu_i^{calc} - \nu_i^{exp}\right) \quad (6)$$

$$\left|\Delta\right|_{max} = max\left|\nu_i^{calc} - \nu_i^{exp}\right| \qquad i = 1,...,M \quad (7)$$

where M is the number of data in the set, $\overline{|\Delta|}$ is the mean absolute difference between the calculated and the experimental values, $\bar{\Delta}$ is the mean difference, $\left|\Delta\right|_{max}$ is the maximum absolute difference.

Graphical animations of the normal modes were built using the Jmol 3D engine (jmol.sourceforge.net;www.theochem.unito.it/crystal_tuto/mssc2013_cd/tutorials/webvib/index.html) and are available on the CRYSTAL Web site (www.crystal.unito.it/animations-of-vibrational-modes.php); this tool is very helpful for a simple and intuitive interpretation of the "nature" of the modes (stretching, bending, libration, translation, etc). Graphs were realised with the Gnuplot utility (www.gnuplot.info).

RESULTS AND DISCUSSION

Structure

Structural parameters of pyrope (Prp) and majorite (Maj) as obtained from our calculations are given in Table 1. Prp has a cubic conventional cell with *Ia-3d* space group symmetry and 4 irreducible atoms; the ordered, lowest energy Mg/Si configuration of Maj was considered in this study, featuring a tetragonal conventional cell, the $I4_1/a$ space group and 13 irreducible atoms.

When compared to structural refinements by Pavese et al. (1995) (Prp) and Angel et al. (1989) (Maj), the computed lattice parameters (i.e. cell edges *a* and *c*) show a slight overestimation of 0.94% (Prp) and 0.96%, 0.54% (Maj), which are in line with the known overestimation due to the adopted functional (see e.g. Dovesi et al. 2011). Atomic fractional coordinates compared to the above mentioned experimental studies show deviations as small as 0.0002÷0.0009 for Prp, and

slightly larger in the case of Maj, where all but one lie in the range 0÷0.0066, with the only larger discrepancy (0.0104) occurring for the *z* coordinate of Mg in site Dod1. These can be considered as quite accurate results, given that previous computational studies of Maj showed deviations in the same range (Vinograd et al. 2006; Yu et al. 2011; Hernández et al. 2015; Pigott et al. 2015).

Vibrational frequencies of pyrope

Symmetry analysis permits to classify the vibrational modes in terms of irreducible representations of the *m3m* point group:

$$3\ A_{1g} \oplus 5\ A_{1u} \oplus 5\ A_{2g} \oplus 5\ A_{2u} \oplus 8\ E_g \oplus 10\ E_u \oplus 14\ F_{1g} \oplus 17\ F_{1u} \oplus 14\ F_{2g} \oplus 16\ F_{2u} \quad (8)$$

There are 17 infrared (IR) active modes with F_{1u} symmetry, and 25 Raman active modes (A_{1g}, E_g and F_{2g} symmetries); the remaining ones are silent.

The computational setup adopted in the present study (B3LYP functional and all electron Gaussian type basis sets) had already been used to analyse the IR (Zicovich et al. 2008; Dovesi et al. 2011) and Raman (Maschio et al. 2013a) properties of Prp. However, at variance with these previous studies, we have here widened the comparison with experiments by including a larger number of datasets, to better assess the accuracy that can be achieved in computational *versus* experimental vibrational spectroscopies.

Vibrational properties of Prp are reported in Tables S1-S5 in the Supplementary Information. Computed IR active frequencies, both Transverse Optical (TO) and Longitudinal Optical (LO) are reported in Table S1 and compared with one experimental study reported by McMillan et al. (1989), three experimental studies carried out by Hofmeister and coworkers (Hofmeister and Chopelas 1991; Hofmeister et al. 1996, 2004) and a lattice dynamics simulation (Chaplin et al. 1998). Statistics on the TO modes (Table S2), as compared with the three datasets by the Hofmeister group, reveal that our simulation has a mean absolute deviation $\overline{|\Delta|}$ in the range 5.2÷6.8 cm^{-1}, and a maximum absolute deviation $|\Delta|_{max}$ of 25.7 cm^{-1}. Interestingly, cross-statistics among the three

datasets by Hofmeister and coworkers show very similar values: $\overline{|\Delta|}$ goes from 4.9 to 6.3 cm^{-1}, while $|\Delta|_{max}$ is as large as 50.0 cm^{-1}. Thus accuracy of our computed IR frequencies is the same than the typical precision of IR measurements carried out on Prp.

The only other theoretical study on Prp that is found is the literature was performed by Chaplin et al. (1998) and made use of lattice dynamics. Compared to the experimental IR-TO datasets, $\overline{|\Delta|}$ ranges from 19.1 to 23.6 cm^{-1}, with a maximum deviation of 44.5 cm^{-1}. These values give evidence for the higher accuracy of *ab initio* B3LYP calculations with respect to classical force field techniques.

Computed Raman frequencies (Table S3) are compared with data from two experimental studies by Hofmeister and coworkers (Hofmeister and Chopelas 1991; Hofmeister et al. 2004), two experimental studies by Kolesov and Geiger (1998, 2000) and once again the lattice dynamics simulation of Chaplin et al. (1998). When comparing our dataset with the experimental ones, $\overline{|\Delta|}$ values (Table S4) fall in the range 4.9÷7.1 cm^{-1}, showing essentially the same accuracy than the IR data. $|\Delta|_{max}$ can be as large as 46.0 cm^{-1}, but it lowers to 25.9 cm^{-1} when considering only the most recent sets from each experimental group. Experimental precision is higher than computational accuracy in the case of Raman, as $\overline{|\Delta|}$ among experimental datasets is only 1.3÷3.9 cm^{-1}, with $|\Delta|_{max}$ of 12.8 cm^{-1}. As for the case of IR-TO frequencies, lattice dynamics simulations (Chaplin et al. 1998) reveal large uncertainties in reproducing the Raman frequencies of Prp.

Vibrational frequencies of majorite

Classification of the modes according to the irreducible representations of the *4/m* point group yields:

$$25\ A_g \square\ 32\ A_u \square\ 27\ B_g \square\ 31\ B_u \square\ 28\ E_g \square\ 33\ E_u \quad (9)$$

The lower symmetry of Maj compared to Prp results in a larger number of distinct vibrational

modes: there are 65 IR active modes (A_u and E_u symmetries), 80 Raman active modes (A_g, B_g and E_g), and 31 silent modes (B_u). Data on the silent modes are reported in Table S6 in the Supplementary Information.

For each one of the 65 IR active modes, Table 2 shows computed TO and LO frequencies together with the corresponding IR absorption intensity. Two experimental datasets are reported, collected by Kato and Kumazawa (1985) and McMillan et al. (1989). Neither of the two experiments registered data below 350 cm^{-1}; our simulation provides information for 22 IR modes in this spectral range. Of the remaining 43 modes above 350 cm^{-1}, the two experiments identify 15 and 22 of them, respectively. A closer look to the data reveals that 5 and 7 experimental peaks (italic values in Table 2), respectively, can be assigned to pairs of computed modes, due to frequency proximity of the latter, thus accounting for part of the modes that are missing in the experiment. Five missing modes (bold values in Table 2) show a quite large intensity, but have not been identified in the experimental curves probably due to superposition with very broad and intense bands; they lie around 480, 845, 915, 928 and 975 cm^{-1}. The remaining missing modes all have relatively low intensities. Comparison between computed and experimental data is very good and of similar quality than for Prp: $\overline{|\Delta|}$ values are 5.7 and 4.6 cm^{-1}, respectively; in both cases only one discrepancy is larger than 10 cm^{-1} (it corresponds to the computed modes at 685 and 989 cm^{-1}, respectively).

Table 3 reports computed Raman frequencies and intensities for the 80 Raman active modes; the former are compared with four experimental datasets, and a DFT-LDA study by Yu et al. (2011). Experiments identified 11 (Manghnani et al. 1998) to 34 (McMillan et al. 1989) peaks; at variance with the IR case, they include data from the whole spectral range from 130 to 1100 cm^{-1}, so that missing peaks are distributed all along this span. Taking as a reference the most complete set by McMillan et al. (1989), we note that as many as 12 experimental frequencies (italic values in Table 3) can be associated to either pairs or triplets of neighbouring computed modes. All the remaining missing modes have relatively low intensity; a look at the spectra in the experimental

papers suggest that these could not be clearly identified due to the low signal-to-noise ratio. Note that three experimental datasets have a spurious frequency in the range 690÷750 cm^{-1}, which could not be assigned to any computed mode. Statistics in Table 4 reveal a very good agreement of our simulated data with the experimental ones, with $\overline{|\Delta|}$ ranging between 3.6 and 4.9 cm^{-1}, the best agreement relating to the most complete dataset by McMillan et al. (1989). Only one computed mode shows discrepancies larger than 10 cm^{-1}, namely the low frequency one at 116.4 cm^{-1} (experiments at 136÷138 cm^{-1}); underestimation of modes in this range has been already reported in the case of Prp (see this study, and Dovesi et al. 2011) and aragonite (De La Pierre et al. 2014).

The DFT study of Yu et al. (2011) reports frequencies for 22 out of 80 Raman active modes. Statistical comparison with the experiments, carried out over the subset of matching frequencies, indicates a slighter worse match than our simulations, with $\overline{|\Delta|}$ between 4.9 and 5.4 cm^{-1}. A look at the dataset in Table 3 shows that 8 out of 22 modes by that study cannot be put in relation with any experimental value, once the latter have been classified by symmetry according to our analysis. The latter has been performed based on symmetry classification of the computed modes (via an algebraic decomposition of the reducible representation built on the basis of the Cartesian atomic coordinates) and on the comparison of computed Raman intensities (a mode with higher computed intensity is more likely to be observed experimentally). This suggests that symmetry labeling by Yu et al. (2011) should be taken with some care. Note that a second set of DFT data on Maj has been published very recently by Hernández et al. (2015), in a study focused on modeling a variety of phases in the MgO-SiO_2 binary system, using the Perdew-Wang '91 GGA functional (Wang and Perdew 1991). Despite their detailed and quite accurate results regarding structural, high pressure, and thermodynamic properties, absolute values for the vibrational frequencies show a large underestimation, around 20 cm^{-1} on average, compared to both our data and the experiments; this is in line with the known trends for the level of theory they adopted.

Overall, the accurate datasets presented here constitute a complete and comprehensive

investigation of the lattice dynamics of end-member Maj, representing a reliable reference not only for spectroscopic and analytical purposes, but also for further thermodynamic investigations.

Isotopic substitution

Simulated isotopic substitution has been applied as a tool to quantitatively characterise the contribution of each chemical species to the vibrational modes of Prp and Maj. To this end, an artificial mass shift of +7.5% has been applied in turn to all atoms of a given species (Mg, Al, Si, or O), that results in negative frequency shifts along the spectral range.

Percent isotopic shifts for Prp are represented in Figure S1 in the Supplementary Information. Let us arbitrarily take a -1% shift as the threshold to identify modes contributed by a given species; then, the 100÷350 cm^{-1} and the 300÷600 cm^{-1} ranges are dominated by Mg and Al, respectively. Of the modes with frequency shift larger than -1% for Si, three lie around 250÷400 cm^{-1}, one lies around 600 cm^{-1}, and the remaining ones are in the range 800÷1100 cm^{-1} (the latter correspond to Si-O stretching modes). Oxygen contributes to the vibrational modes along the whole spectral range.

Simulated isotopic substitution applied to Maj results in the frequency shifts represented in Figure 1. Taking again a threshold of -1%, Maj shows features similar to Prp when dodecahedral Mg, tetrahedral Si and O are considered; in particular, dodecahedral Mg can be associated to modes in the 100÷400 cm^{-1} range, and tetrahedral Si to two modes around 300÷400 cm^{-1}, to one mode at about 600 cm^{-1}, and to the range 800÷1100 cm^{-1}. Two separate substitutions were carried out for Mg and Si occupying the octahedral sites. Octahedral Mg can be strictly related to three modes in the range 300÷450 cm^{-1}; if a slightly lower threshold is considered, around -0.75%, then the larger 250÷500 cm^{-1} range can be assigned, moved to higher frequencies with respect to the dodecahedral Mg range. Octahedral Si relates to the 450÷750 cm^{-1} range, at lower frequencies than the principal tetrahedral Si range. Note how the two species occupying octahedral sites can be assigned to rather distinct spectral ranges.

306

307 ***IR spectra***

308 Computed IR spectra of Prp and Maj are represented in Figure 2, as blue and red curves,
309 respectively.

310 All modes above 750 cm^{-1} are pure internal Si-O stretchings of the SiO_4 tetrahedra; there are 3
311 and 12 IR active modes in this range in Prp and Maj, respectively (see Table S1 and Table 2). These
312 modes are both limited in number and perturbed by a little extent by the structural differences
313 between Prp and Maj; thus it is possible to establish relations between the two garnets, by
314 exploiting correlation rules of irreducible representations (see e.g. Ferraro and Ziomek 1975): A_{1u}
315 and A_{2u} modes in Prp relate to A_u and B_u modes in Maj, respectively; E_u modes split into pairs of A_u
316 and B_u modes; F_{1u} and F_{2u} modes turn into pairs of $A_u + E_u$ and $B_u + E_u$ modes, respectively.
317 Correspondences are summed up in Table 5. Out of the 10 peaks visible in the IR spectrum of Maj,
318 6 of them are 3 pairs of A_u and E_u modes that can be related to the 3 F_{1u} peaks of Prp. The other 4
319 visible peaks relate to silent modes in Prp: 3 E_u modes at 876, 915 and 954 cm^{-1} (resulting from F_{2u}
320 modes of Prp) and 1 A_u mode at 928 cm^{-1}, related to the E_u mode at 913 cm^{-1} of Prp.

321 The frequency range below 750 cm^{-1} features a large number of modes involving motions of
322 cations in the dodecahedral and octahedral sites, so that correspondences between the two spectra
323 are loosened and of little significance. Given the variety of structural motions involved in this
324 spectral range, it is interesting to characterise the most relevant peaks in the two spectra in terms of
325 the structural subunits dominating the corresponding normal modes. Both simulated isotopic
326 substitution (discussed above) and graphical inspection of the modes (see CRYSTAL Web site,
327 www.crystal.unito.it/animations-of-vibrational-modes.php) can be used to this end. Results are
328 summarised in Table S7 in the Supplementary Information. Of the 5 intense modes in the spectrum
329 of Prp, the three low frequency ones at 119, 187 and 333 cm^{-1} relate to Mg cations motions, with
330 the latter also involving translations of the SiO_4 tetrahedra; the remaining high frequency ones at
331 380 and 458 cm^{-1} are motions of the Al cations, coupled with rocking motions of the SiO_4

tetrahedra. In the case of Maj, starting from the lower frequencies, the four intense modes in the range 340÷370 cm^{-1} (labelled as 21, 22, 23 and 25 in Table 2) are related to Mg motions in both dodecahedral and octahedral sites, coupled with SiO_4 librations and either translations or rockings. The three intense modes in the range 380÷400 cm^{-1} (28, 30 and 31 in Table 2) relate to Mg motions only in the octahedral sites, coupled with SiO_4 librations and rockings. The very intense mode at 441 cm^{-1} involves motions of all the structural subunits. Finally, the two intense modes at 510 and 550 cm^{-1} relate to motions of the Si atoms in the octahedral sites, coupled with SiO_4 librations and rockings. Note the variety of structural motions in the case of Maj, arising from the octahedral sites being occupied by both Mg and Si atoms.

Raman spectra

Computed Raman spectra are shown in Figure 3. Starting from the high frequency range above 750 cm^{-1}, Prp and Maj have 6 and 18 Raman active modes, respectively, 4 and 11 of which are visible in the spectrum (see Table 5 for symmetry correspondences). In particular, 8 visible modes of Maj are in relation with active modes of Prp: the highly intense A_{1g} peak of Prp at 927 cm^{-1} relates to the A_g peak of Maj at 926 cm^{-1}; the relatively intense peak of Prp at 864 cm^{-1} is the superposition of a F_{2g} and a E_g mode and results in four low intensity peaks in Maj (1 A_g, 2 B_g and 1 E_g), spread over the range 810÷880 cm^{-1}; the small F_{2g} peaks of Prp at 899 and 1072 cm^{-1} relate to the small E_g peaks of Maj at 910 and 1070 cm^{-1}; the A_g peak of Maj at 960 cm^{-1} comes from a little E_g feature of Prp at 939 cm^{-1} (hidden by the very intense mode at 927 cm^{-1}). The remaining 3 visible modes of Maj result from silent Prp modes: the A_g mode representing the largest contribution to the peak found at 886 cm^{-1} relates to the F_{1g} silent mode of Prp at 887 cm^{-1}; the two small peaks at 796 cm^{-1} (A_g) and 803 cm^{-1} (E_g) both relate to the F_{1g} silent mode of Prp at 848 cm^{-1}.

As regards the spectral range below 750 cm^{-1}, isotopic substitution and graphical animation of the modes can be used again to inspect the nature of the corresponding vibrational modes. Findings are reported in Table S8 in the Supplementary Information. Of the 6 intense peaks of Prp the first

two, at 208 and 338 cm^{-1}, correspond to Mg motions coupled with SiO_4 librations; the two intense peaks at 357 and 566 cm^{-1} are pure SiO_4 librations; the two small peaks at 515 and 657 cm^{-1} are rocking motions of the SiO_4 tetrahedra. In the case of Maj, of the 11 modes which contribute to the most intense features in the spectrum, the 4 ones in the range 150÷230 cm^{-1} (labelled as 3, 4, 7 and 13 in Table 3) and the one at 369 cm^{-1} are Mg motions coupled with SiO_4 librations. The small peaks at 317 and 402 cm^{-1} as well as the very intense mode at 602 cm^{-1} are pure SiO_4 librations. Finally, the three small peaks at 458, 541 and 653 cm^{-1} are SiO_4 rocking motions. Note how, despite differences in peak positions and intensities, the Raman spectrum in the low frequency domain presents similar structural contributions in Prp and Maj.

High pressure vibrational properties and mode Grüneisen parameters

Mode Grüneisen parameters allow us to test the accuracy of our simulations at high pressure conditions, through direct comparison with the experimental data available for both Prp (Chopelas 2006) and Maj (Rauch et al. 1996; Manghnani et al. 1998; Chopelas 1999). Data for the Raman modes can be found in Table S9 in the Supplementary Information and Table 6 in the case of Prp and Maj, respectively; data for the remaining modes are reported in Tables S5, S6, S10, S11 in the Supplementary Information. Accurate mode Grüneisen parameters are crucial to determine fundamental thermodynamic properties, such as thermal expansion (Ottonello et al. 2010a, 2013; Prencipe et al. 2011; Erba 2014; Belmonte et al. 2014; Ulian and Valdrè 2015).

The mode Grüneisen parameters calculated for Prp and Maj up to pressures of 25 GPa compare well with available experimental data, except for some low frequency modes displaying relatively large values, up to 3.7 for Prp and 3.5 for Maj in the frequency ranges 105 – 119 cm^{-1} and 101 – 116 cm^{-1}, respectively; the corresponding experimental data are no larger than 1.9 and 1.8, respectively. Note that in the case of Maj the relatively large computed γ values are in excellent agreement with the very recent GGA results by Hernández et al. (2015) (see their Supplementary content): compare our values of 3.51 and 3.36 for the two lowest frequency modes, namely the IR

active E_u mode at 101 cm^{-1} and the Raman active E_g mode at 116 cm^{-1}, respectively, with the literature values of 3.50 and 3.59. Furthermore, the Raman spectra measured for Maj by Manghnani et al. (1998) and Chopelas (1999) reveal that the lowest frequency experimental modes, observed in the range 136 − 220 cm^{-1}, have γ values twice as large than the medium-to-high frequency modes (and the averaged γ_i, as well). Although mode Grüneisen parameters sensibly greater than 1.0 are possible (see for instance Lu et al. 2012), the apparently anomalous values associated with the vibrational modes with lowest frequencies may have a lattice dynamical justification. In particular, the mismatch between the relatively small Mg^{2+} cation and the size of the dodecahedral sites in the garnet structure is the most cited cause for the strongly anisotropic character of the thermal motions of these modes (Armbruster et al. 1992; Pavese et al. 1995; Kolesov and Geiger 2000); anharmonic effects could become relevant in this context (Winkler et al. 2000). The fact that both in Prp and Maj these modes are dominated by motions of Mg atoms in the dodecahedral sites, as confirmed by the analysis in the Isotopic Substitution Section above, clearly supports this interpretation.

Apart from the case of the just discussed low frequency modes (which represent only the 2% of all the modes), our calculated high pressure properties are in very good agreement with experimental results. In particular, Figure 4 shows the calculated pressure dependence for all the Raman active modes of Maj (A_g, B_g and E_g symmetries) up to 25 GPa, as compared with the experimental measurements by Rauch et al. (1996), Manghnani et al. (1998) and Chopelas (1999). It turns out that all the vibrational frequencies increase linearly with pressure (and so all the mode Grüneisen parameters are positive). By comparing the numerical values of both γ and dv/dP for the Raman modes of Maj, as reported in Table 6, we may conclude that there is a general agreement between experiment and simulation, within the limits of experimental and/or computational uncertainty; the former is related to possible impurities in the samples (e.g. hydroxyl groups), cation disorder, instrumental setup, whereas the latter mainly to the choice of the exchange-correlation functional. A relevant feature of the high pressure Raman spectra of Maj is the large value of the dv/dP slopes characterising the high frequency bands in three different experimental studies (Rauch

et al. 1996, Manghnani et al. 1998, Chopelas 1999). These slopes are between 3.7 and 4.3 cm^{-1}/GPa in the frequency range above 750 cm^{-1}, whereas they never exceed 2.55 cm^{-1}/GPa in the range below 750 cm^{-1}. Our calculated $d\nu/dP$ slopes confirm this point: they lie within 3 and 5 cm^{-1}/GPa in the high frequency range, and they rarely exceed 3 cm^{-1}/GPa in the low-to-medium frequency range.

Finally, using the mode Grüneisen parameters we have computed the cell volumes of Prp and Maj as corrected for vibrational effects at 300 K and 1 bar; the corresponding volume expansions amount to 0.21% and 0.24%, respectively. The average value for the mode Grüneisen parameters of both minerals is about 1; this value can be used (see Aliatis et al. 2015) to estimate that the change in frequencies related to these volume expansions is about -0.2%. Thus frequency corrections due to vibrational pressure lie between 0 and -2 cm^{-1} when spanning the spectral range from the lowest frequency to the highest. We have mentioned above that a few modes in the range 100 – 120 cm^{-1} have peculiarly large mode Grüneisen parameters, up to 3.7; the corresponding maximum frequency correction for these modes is about -1 cm^{-1} (-0.8%).

IMPLICATIONS

In this work the vibrational properties of majorite-pyrope garnet end-members have been thoroughly investigated both at ambient and high pressure conditions by means of *ab initio* quantum mechanical simulations. An accurate and complete dataset of vibrational spectroscopic properties for majorite has been presented here for the first time, alongside the corresponding dataset for pyrope.

The present detailed analysis is particularly relevant in the case of the majorite end-member, for whose vibrational spectrum no complete experimental characterisation is available. Thermal expansivity (α_V) is among the thermodynamic properties stemming from vibrational frequencies and mode Grüneisen parameters of crystalline phases (see Anderson 1995 for details). Together with density, this quantity is of fundamental importance for the physical and compositional models

436 of the Earth's interior, since it controls the buoyancy forces that drive thermal convection in the
437 mantle (Christensen 1995).

438 Despite the fact that majorite is a major constituent of the mantle transition zone, thermal
439 expansivity values for this mineral are poorly constrained by experiments due to several technical
440 problems, so that their extrapolation at high pressure and temperature conditions is affected by large
441 uncertainties. A survey of the literature values clearly shows a high degree of scattering, with α_V
442 ranging from 1.6×10^{-5} K^{-1} (Jacobs and de Jong 2007) to 2.2×10^{-5} K^{-1} (Fabrichnaya et al. 2004) at
443 298.15 K and 1 bar, according to different thermodynamic assessments. This is the reason why, in
444 most numerical simulations of mantle convection, either the thermal expansivity of majorite is
445 assumed constant or only its pressure dependence is taken into account, by means of simplified
446 parameterizations relying on extrapolations of low pressure data (Schmeling et al. 2003; Tosi et al.
447 2013).

448 Due to the lack of experimental data, computational modelling is the best way to obtain
449 reliable and physically consistent values for the thermal expansivity of majorite at high pressure and
450 high temperature conditions. Employing the dataset of vibrational properties presented in this paper,
451 a value of 2.1×10^{-5} K^{-1} can be calculated for α_V at room pressure and temperature conditions. This
452 value lies within the range of the current thermodynamic databases for geophysical modelling and
453 is in good agreement with the lattice dynamics calculation by Chopelas et al. (2000) (i.e. 2.24×10^{-5}
454 K^{-1}) and the first principles GGA calculations by Hernandez et al. (2015) (i.e. 2.15×10^{-5} K^{-1}). In
455 contrast, DFT simulations by Yu et al. (2011) using both LDA and GGA give sensibly
456 overestimated values, namely 2.5×10^{-5} K^{-1} and 2.9×10^{-5} K^{-1}, respectively. Most importantly, if high
457 pressure and high temperature conditions are considered, α_V values currently adopted for majorite
458 in thermodynamic databases (cf. Fabrichnaya et al. 2004; Jacobs and de Jong 2007) seem to be
459 drastically underestimated. By way of example, let us consider the pressure and temperature
460 conditions relevant for the bottom part of the mantle transition zone. At 1500 K and 20 GPa, the
461 thermodynamic tabulations by Fabrichnaya et al. (2004) give $\alpha_V \cong 0.7\times10^{-5}$ K^{-1}. Using our first

462 principle results, the value obtained at the same conditions is 2.2×10^{-5} K^{-1}, i.e. more than three
463 times as large. The high quality data presented here therefore represent the ideal starting point for
464 an extensive revision of the thermodynamic and thermoelastic properties of mantle minerals at deep
465 Earth's conditions, aimed at improving the numerical modelling of thermo-chemical convection in
466 the mantle.
467

468 **ACKNOWLEDGMENTS**

469 The authors are thankful to the reviewers of the manuscript for their useful observations. This
470 research was supported by computational resources provided by the Pawsey Supercomputing
471 Centre (funded from the Australian Government and the Government of Western Australia) and the
472 Australian National Computational Infrastructure (NCI, funded by the Australian Government).
473 Financial support by the University of Genova (Progetto di Ateneo 2013 and 2014 to DB) is also
474 gratefully acknowledged.
475

476 **TABLES**

477

Prp					Maj				
		a		V			a	c	V
Cell		11.546		1539.19	Cell		11.611	11.543	1556.19
Atom	Site	*x*	*y*	*z*	Atom	Site	*x*	*y*	*z*
Mg	Dod1	0.125	0	0.25	Mg	Dod1	0.6293	0.0147	0.2691
					Mg	Dod2	0.5	0.25	0.6232
Al	Oct1	0	0	0	Mg	Oct1	0.5	0	0.5
					Si	Oct2	0.5	0	0
Si	Tet1	0.375	0	0.25	Si	Tet1	0.5	0.25	0.375
					Si	Tet2	0.5	0.25	0.875
					Si	Tet3	0.6249	0.0107	0.7560
O	O(1)	0.0323	0.0498	0.6535	O	O(1)	0.5251	0.0574	0.6680
					O	O(2)	0.5437	-0.0450	0.8605
					O	O(3)	0.7238	0.1060	0.8045
					O	O(4)	0.7133	-0.0847	0.7025
					O	O(5)	0.4377	0.1629	0.4688
					O	O(6)	0.3979	0.2146	0.7823

478 **Table 1** Calculated structural properties of pyrope and majorite. Cell parameters and cell volume
479 are in Å and $Å^3$, respectively; atomic positions are expressed as fractional coordinates.

480

481

482

483

484

485

486

487

488

489

490

491

#	Sym	$\nu_{TO,calc}$	II_{calc}	$\nu_{TO,exp}$ Kato '85	$\nu_{TO,exp}$ McMillan '89	$\nu_{LO,calc}$	#	Sym	$\nu_{TO,calc}$	II_{calc}	$\nu_{TO,exp}$ Kato '85	$\nu_{TO,exp}$ McMillan '89	$\nu_{LO,calc}$
1	E_u	101.3	1030			114.6	36	E_u	457.6	1111	*458*	*459*	454.3
2	E_u	130.9	175			134.1	37	A_u	464.0	186			466.5
3	A_u	142.4	730			148.5	38	A_u	**479.8**	**544**			486.3
4	A_u	156.4	673			178.4	39	E_u	491.1	780		490	482.3
5	E_u	172.3	577			177.7	40	E_u	504.3	248	*501*	*501*	500.6
6	A_u	191.8	44			193.6	41	A_u	510.3	2172			555.0
7	E_u	197.7	170			198.7	42	E_u	522.5	1278	520	521	509.5
8	E_u	206.8	679			213.0	43	E_u	550.1	2112	549	549	534.8
9	A_u	213.4	94			215.5	44	A_u	563.2	55			565.7
10	E_u	222.5	140			224.1	45	A_u	579.7	278	*576*	*580*	585.2
11	E_u	240.2	307			242.4	46	E_u	583.2	608			576.1
12	A_u	247.1	388			253.3	47	A_u	599.6	832		604	637.8
13	E_u	257.3	829			264.5	48	E_u	636.8	510	627	632	612.3
14	A_u	258.8	1			258.8	49	A_u	656.7	4			656.9
15	E_u	277.0	62			277.6	50	E_u	684.8	200	670	675	687.4
16	A_u	289.8	386			294.2	51	A_u	701.6	82	693	693	703.4
17	E_u	300.3	336			302.3	52	E_u	706.8	31			707.1
18	A_u	312.1	78			312.8	53	A_u	730.4	32			730.9
19	A_u	322.6	57			323.1	54	E_u	826.3	8316	831	827	860.3
20	E_u	325.8	403			327.4	55	A_u	**845.1**	**469**			847.3
21	E_u	341.4	1119			346.1	56	E_u	876.1	1256	*876*	*879*	885.1
22	A_u	345.1	1234			350.5	57	A_u	886.4	6185			1071.5
23	A_u	360.5	1596			373.7	58	E_u	901.4	2437	903	906	935.0
24	E_u	361.7	213		*354*	362.2	59	E_u	**915.1**	**478**			912.7
25	E_u	368.8	1052		362	372.0	60	A_u	**928.4**	**1011**			920.2
26	A_u	372.4	22			371.7	61	A_u	950.4	48			949.5
27	A_u	379.6	579			388.3	62	E_u	954.2	793	950	954	961.8
28	E_u	384.9	2453		*383*	391.4	63	A_u	**974.5**	**1357**			958.4
29	A_u	392.1	35			392.5	64	E_u	989.1	3867	998	1002	1067.2
30	E_u	396.5	1174			404.6	65	A_u	1055.5	37			1051.5
31	A_u	399.0	980	*395*	*398*	440.7	M				15	22	
32	E_u	417.1	1079		416	421.7	$\overline{\lvert\Delta\rvert}$				5.7	4.6	
33	Au	425.5	317		433	418.7	$\overline{\Delta}$				3.5	1.1	
34	Eu	440.5	4968	442	446	648.7	$\lvert\Delta\rvert_{max}$				14.8	12.9	
35	Au	452.7	21			453.1							

Table 2 Calculated and experimental IR properties of majorite. ν and II are the frequencies [cm^{-1}] and absorption integrated intensities [km/mol], respectively. Frequencies of both TO and LO modes are given. Statistical indices (defined in the Computational Method Section) are reported on bottom. Experimental frequencies in italic are assigned to pairs of contiguous computed modes (the most

496 intense one has been chosen to compute statistics); calculated frequencies in bold correspond to
497 intense peaks not identified in the experiments.
498

#	Sym	ν_{calc}	II_{calc}	ν_{exp} McMillan '89	Rauch '96	Manghnani '98	Chopelas '99	ν_{calc} Yu '11
1	E_g	116.4	87	138			136	130.34
2	E_g	138.0	9					
3	B_g	154.2	147	*159*				
4	A_g	154.5	165					
5	E_g	162.9	2					
6	B_g	164.6	6					
7	A_g	177.5	265	181				
8	E_g	189.6	96	*197*	196.1	*197*	*195*	198.90
9	B_g	200.1	45		200.0			194.46
10	A_g	210.3	30	205				
11	E_g	211.8	6					214.84
12	B_g	212.1	2					
13	A_g	229.7	369	226	222.0	222	226	
14	E_g	237.2	105	*238*	*233.9*			
15	B_g	242.4	79					237.82
16	A_g	256.9	49	261	255.2			252.27
17	E_g	257.4	5					
18	A_g	276.4	28	*275*	*273.2*		*277*	281.34
19	B_g	281.6	24					
20	E_g	298.0	11	*293*				
21	B_g	299.0	39					
22	E_g	308.3	24					
23	B_g	315.7	19					320.71
24	A_g	315.9	0					
25	A_g	317.1	146	311	307.9		311	313.30
26	E_g	320.5	9					
27	A_g	338.8	33	336	332.4		334	342.43
28	E_g	344.1	16					
29	B_g	346.7	12					
30	B_g	352.8	60	*354*	*354.9*	*359*		351.55
31	E_g	357.3	29					
32	E_g	363.9	11					372.98
33	B_g	367.4	51	*367*	*365.9*		*367*	
34	A_g	368.9	229					
35	B_g	382.5	3					
36	E_g	393.1	24					398.57
37	A_g	396.9	17					

38	A_g	402.3	113	398	396.6		398	
39	B_g	407.1	25					
40	E_g	413.4	1					
41	A_g	429.8	53	429	427.8			428.33
42	A_g	458.0	116	458	456.4	456	458	
43	E_g	462.2	20					
44	B_g	466.5	3					459.95
45	E_g	481.2	8	*481*				
46	B_g	482.9	5					
47	B_g	500.4	59	498	493.6			
48	A_g	506.0	33	507	515.8			
49	E_g	509.7	1					
50	A_g	532.3	11					
51	E_g	540.6	110	535	533.1			
52	B_g	559.4	60	*559*	*554.0*			
53	A_g	567.7	59					
54	B_g	585.7	18					
55	E_g	593.0	6					
56	A_g	602.0	1667	602	599.0	597	602	
57	E_g	611.3	21					
58	B_g	622.2	9					607.77
59	A_g	636.5	2			*641*		
60	B_g	639.1	16					
61	E_g	653.2	197	648	646.7		648	
62	B_g	670.7	66					649.49
	?	--	--	724		743	690	
63	A_g	795.9	79					804.06
64	E_g	802.5	139	802	800.0	797	802	
65	B_g	812.9	72					
66	E_g	850.0	97	852	852.8			
67	A_g	867.2	181	873				
68	B_g	878.6	89					
69	A_g	886.2	399					
70	B_g	886.9	65	*889*	*884.7*	*885*	*889*	893.12
71	E_g	888.4	45					
72	E_g	909.8	110					
73	A_g	926.1	1938	931	929.6	928	931	921.72
74	B_g	957.0	28					
75	A_g	960.2	222	964	964.0			966.43
76	E_g	984.5	7	*989*				
77	A_g	986.4	9					
78	B_g	1029.6	14	1034				
79	E_g	1069.6	214	*1065*	*1064.7*	*1058*		
80	B_g	1073.0	57					1067.28

Table 3 Calculated and experimental Raman properties of majorite. ν and II are the frequencies

500 [cm^{-1}] and isotropic integrated intensities (in arbitrary units), respectively. Experimental
501 frequencies in italic are assigned to pairs or triplets of contiguous computed modes (the most
502 intense one has been chosen to compute statistics).
503

		McMillan '89	Rauch '96	Manghnani '98	Chopelas '99	Yu '11
This work	M	33	25	10	14	22
	$\overline{\lvert\Delta\rvert}$	3.6	4.4	4.9	4.3	6.8
	$\overline{\Delta}$	-0.3	2.1	2.4	0.3	-0.1
	$\lvert\Delta\rvert_{max}$	21.6	9.8	11.6	19.6	21.2
McMillan '89	M	--	24	9	14	10
	$\overline{\lvert\Delta\rvert}$	--	2.7	3.9	0.6	4.9
	$\overline{\Delta}$	--	1.6	2.8	0.3	1.4
	$\lvert\Delta\rvert_{max}$	--	8.8	7.0	2.0	9.3
Rauch '96	M	--	--	9	13	10
	$\overline{\lvert\Delta\rvert}$	--	--	2.3	2.6	4.9
	$\overline{\Delta}$	--	--	1.4	-1.8	-1.0
	$\lvert\Delta\rvert_{max}$	--	--	6.7	5.0	10.0
Manghnani '98	M	--	--	--	7	3
	$\overline{\lvert\Delta\rvert}$	--	--	--	3.6	5.4
	$\overline{\Delta}$	--	--	--	-3.0	5.4
	$\lvert\Delta\rvert_{max}$	--	--	--	5.0	7.4
Chopelas '99	M	--	--	--	--	6
	$\overline{\lvert\Delta\rvert}$	--	--	--	--	5.1
	$\overline{\Delta}$	--	--	--	--	0.1
	$\lvert\Delta\rvert_{max}$	--	--	--	--	9.3

504 **Table 4** Statistics on the calculated and experimental Raman frequencies [cm^{-1}] of majorite (data in
505 Table 3). Statistical indices are defined in the Computational Method Section.
506
507
508
509

IR						Raman					
Prp			Maj			Prp			Maj		
ν_{calc}	Sym	II_{calc}	ν_{calc}	Sym	II_{calc}	ν_{calc}	Sym	II_{calc}	ν_{calc}	Sym	II_{calc}
867.9	**F_{1u}**	**13959**	**826.3**	**E_u**	**8316**	847.7	F_{1g}		**795.9**	**A_g**	**79**
			845.1	**A_u**	**469**				**802.5**	**E_g**	**139**
869.8	F_{2u}		821.2	B_u		**863.9**	**F_{2g}**	**510**	**812.9**	**B_g**	**72**
			876.1	**E_u**	**1256**				**850.0**	**E_g**	**97**
898.6	**F_{1u}**	**5793**	**886.4**	**A_u**	**6185**	865.0	E_g	48	**867.2**	**A_g**	**181**
			901.4	**E_u**	**2437**				**878.6**	**B_g**	**89**
907.2	A_{2u}		878.5	B_u		887.1	F_{1g}		**886.2**	**A_g**	**399**
912.8	E_u		925.5	B_u					888.4	E_g	45
			928.4	**A_u**	**1011**	**899.2**	**F_{2g}**	**47**	886.9	B_g	65
915.0	F_{2u}		**915.1**	**E_u**	**478**				**909.8**	**E_g**	**110**
			937.7	B_u		**926.6**	**A_{1g}**	**3072**	**926.1**	**A_g**	**1938**
937.1	E_u		950.4	A_u	48	939.2	E_g	19	957.0	B_g	28
			951.9	B_u					**960.2**	**A_g**	**222**
956.1	F_{2u}		**954.2**	**E_u**	**793**	975.5	F_{1g}		984.5	E_g	7
			980.4	B_u					986.4	A_g	9
972.8	**F_{1u}**	**5920**	**974.5**	**A_u**	**1357**	1032.9	A_{2g}		1029.6	B_g	14
			989.1	**E_u**	**3867**	**1072.3**	**F_{2g}**	**295**	**1069.6**	**E_g**	**214**
1052.5	A_{1u}		1055.5	A_u	37				1073.0	B_g	57

Table 5 Correspondences between modes of pyrope and majorite in the high frequency range (above 750 cm^{-1}) of the IR and Raman spectra. Modes in bold are the ones distinguishable in the spectra (see Figures 2 and 3).

#	Sym	ν_{calc}	dv/dP_{calc}	dv/dP_{exp} Rauch '96	dv/dP_{exp} Manghnani '98	dv/dP_{exp} Chopelas '99	dv/dP_{calc} Yu '11	γ_{calc}	γ_{exp} Manghnani '98	γ_{exp} Chopelas '99	γ_{calc} Yu '11
1	E_g	116.4	2.51			1.61	1.51	3.36		1.77	1.86
2	E_g	138.0	1.72					1.94			
3	B_g	154.2	0.22					0.22			
4	A_g	154.5	2.06					2.08			
5	E_g	162.9	1.49					1.43			
6	B_g	164.6	2.68					2.54			
7	A_g	177.5	1.57					1.38			
8	E_g	189.6	1.87	0.92			1.27	1.54			1.03
9	B_g	200.1	1.21	0.72	0.99	1.20	1.47	0.94	0.84	0.90	1.22
10	A_g	210.3	0.49					0.36			
11	E_g	211.8	2.27				1.97	1.67			1.47
12	B_g	212.1	2.08					1.53			
13	A_g	229.7	2.02	1.98	2.11	1.97		1.37	1.56	1.32	
14	E_g	237.2	1.93	1.25				1.27			
15	B_g	242.4	1.96				1.80	1.26			1.22
16	A_g	256.9	1.48	1.9			1.30	0.90			0.83
17	E_g	257.4	2.98					1.81			
18	A_g	276.4	1.52	1.69		1.70	1.67	0.86		0.97	0.95
19	B_g	281.6	1.46					0.81			
20	E_g	298.0	1.75					0.92			
21	B_g	299.0	1.88					0.98			
22	E_g	308.3	2.47					1.25			
23	B_g	315.7	3.21				2.21	1.59			1.11
24	A_g	315.9	3.92					1.93			
25	A_g	317.1	1.83	1.73		1.90	1.53	0.90		0.92	0.79
26	E_g	320.5	1.46					0.71			
27	A_g	338.8	2.33	2.17		2.53	2.20	1.07		1.14	1.03
28	E_g	344.1	2.32					1.05			
29	B_g	346.7	4.61					2.08			
30	B_g	352.8	2.34	2.05	1.65		1.91	1.04	0.74		0.87
31	E_g	357.3	2.50					1.09			
32	E_g	363.9	2.31				2.08	0.99			0.90
33	B_g	367.4	3.25					1.38			
34	A_g	368.9	2.73	2.6		2.32		1.15		0.95	
35	B_g	382.5	2.84					1.16			
36	E_g	393.1	2.77				2.00	1.10			0.81
37	A_g	396.9	2.63					1.04			
38	A_g	402.3	1.64	2.7		2.34		0.64		0.54	
39	B_g	407.1	2.59					0.99			
40	E_g	413.4	1.66					0.63			
41	A_g	429.8	2.37	2.1			2.77	0.86			1.04
42	A_g	458.0	1.31	1.62	1.91	1.83		0.45	0.69	0.60	

43	E_g	462.2	2.14					0.72			
44	B_g	466.5	1.83				1.52	0.61			0.53
45	E_g	481.2	1.55					0.50			
46	B_g	482.9	2.26					0.73			
47	B_g	500.4	1.57	1.44				0.49			
48	A_g	506.0	2.32	1.61				0.72			
49	E_g	509.7	2.37					0.73			
50	A_g	532.3	2.50					0.73			
51	E_g	540.6	2.29	2.11				0.66			
52	B_g	559.4	2.27	2.5				0.63			
53	A_g	567.7	2.60					0.72			
54	B_g	585.7	1.61					0.43			
55	E_g	593.0	2.62					0.69			
56	A_g	602.0	3.18	2.49	2.54	2.51		0.83	0.70	0.63	
57	E_g	611.3	2.86					0.73			
58	B_g	622.2	2.67				2.38	0.67			0.63
59	A_g	636.5	2.04		2.43			0.50	0.63		
60	B_g	639.1	1.51					0.37			
61	E_g	653.2	2.25	2.31		2.34		0.54		0.54	
62	B_g	670.7	2.35				2.14	0.55			0.53
63	A_g	795.9	4.21				3.88	0.83			0.78
64	E_g	802.5	4.20	3.8	4.29	3.39		0.82	0.89	0.63	
65	B_g	812.9	3.61					0.69			
66	E_g	850.0	5.95	3.9				1.09			
67	A_g	867.2	3.27					0.59			
68	B_g	878.6	5.78					1.03			
69	A_g	886.2	3.79	3.8	3.91	3.93		0.67	0.72	0.66	
70	B_g	886.9	4.75				4.00	0.84			0.72
71	E_g	888.4	4.34					0.76			
72	E_g	909.8	4.86					0.83			
73	A_g	926.1	4.59	3.7	3.67	4.20	3.56	0.77	0.66	0.67	0.62
74	B_g	957.0	4.86					0.79			
75	A_g	960.2	5.29	3.9			3.81	0.86			0.63
76	E_g	984.5	5.45					0.86			
77	A_g	986.4	5.56					0.88			
78	B_g	1029.6	5.09					0.77			
79	E_g	1069.6	5.13	4.1	3.72			0.75	0.59		
80	B_g	1073.0	5.07				3.91	0.74			0.59
$\overline{\gamma}$								1.02	0.81	0.87	0.92

Table 6 Calculated and experimental mode Grüneisen parameters γ (dimensionless) and pressure dependences dv/dP [cm^{-1}/GPa] for the Raman modes of majorite. $\overline{\gamma}$ is the mean value computed over each set of γ data.

FIGURES

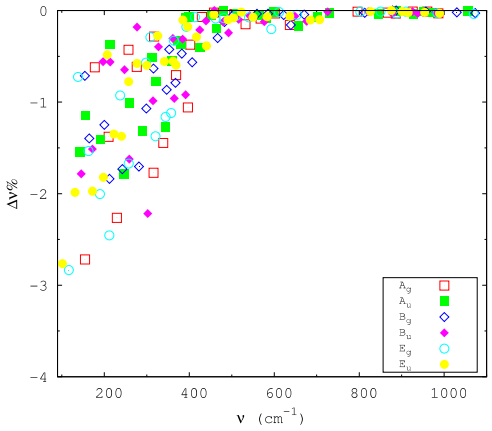

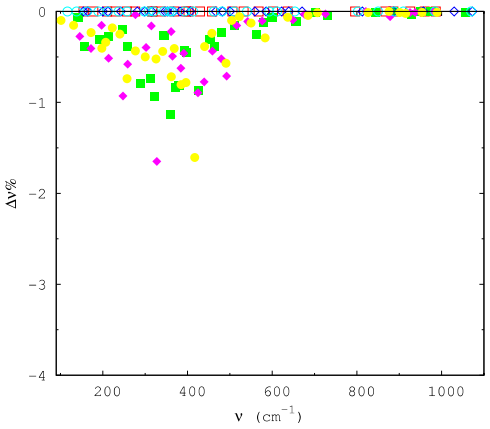

(a) Mg (dodecahedral site) (b) Mg (octahedral site)

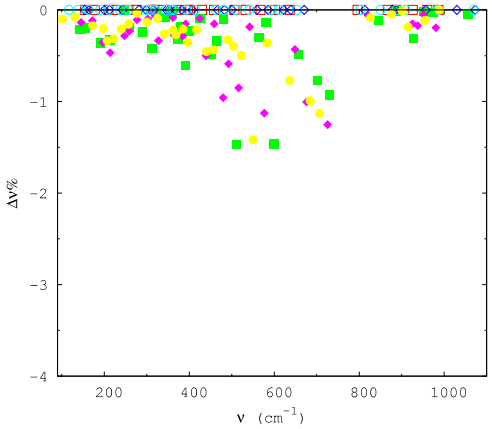

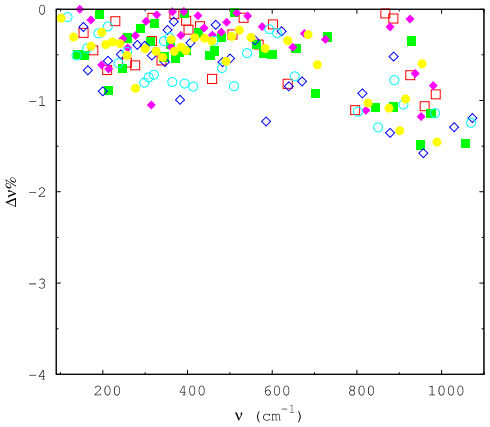

(c) Si (octahedral site) (d) Si (tetrahedral site)

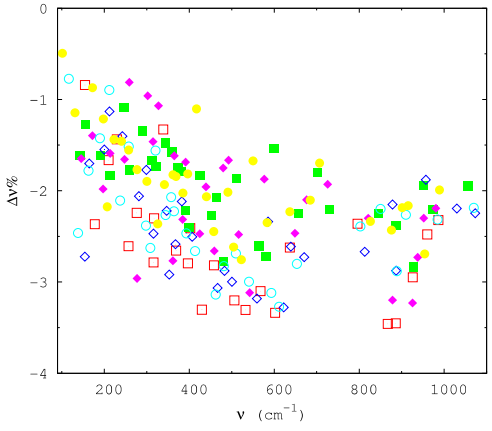

(e) O

534 **Figure 1** Percentage isotopic shifts Δν % on the vibrational frequencies of majorite. Masses of each
535 species have been in turn increased by 7.5%.

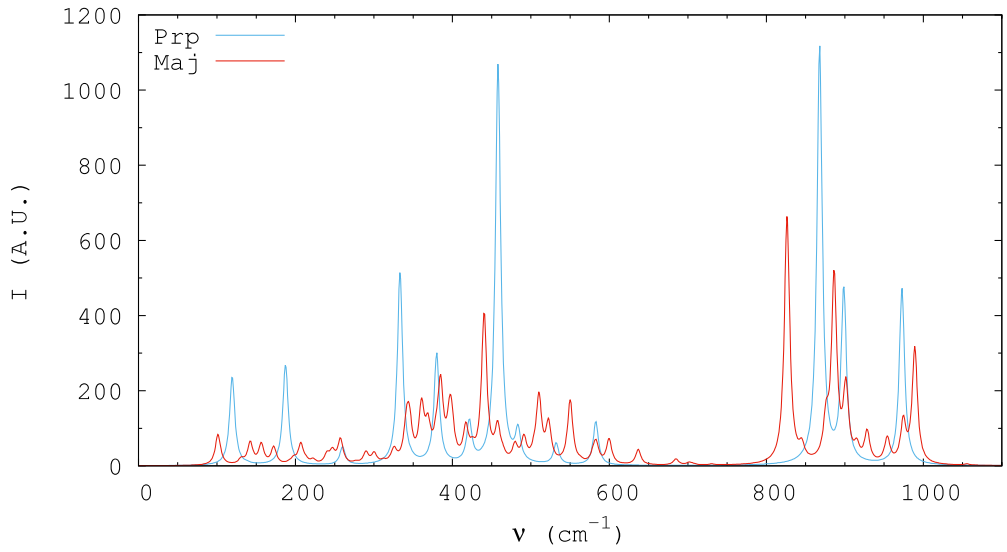

536

537

538 **Figure 2** Computed IR spectra of pyrope and majorite. The peak integrated intensity of each *n-th*
539 mode is II_n [km/mol] (see Tables S1 and 2).

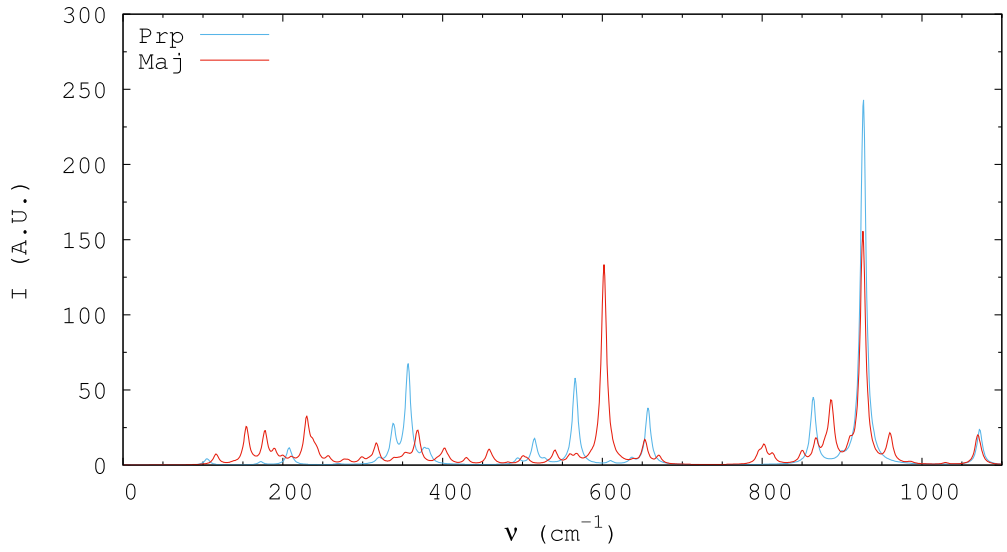

540

541 **Figure 3** Computed Raman spectra of pyrope and majorite. The peak integrated intensity of each *n-*
542 *th* mode is II_n (in arbitrary units, see Tables S3 and 3).

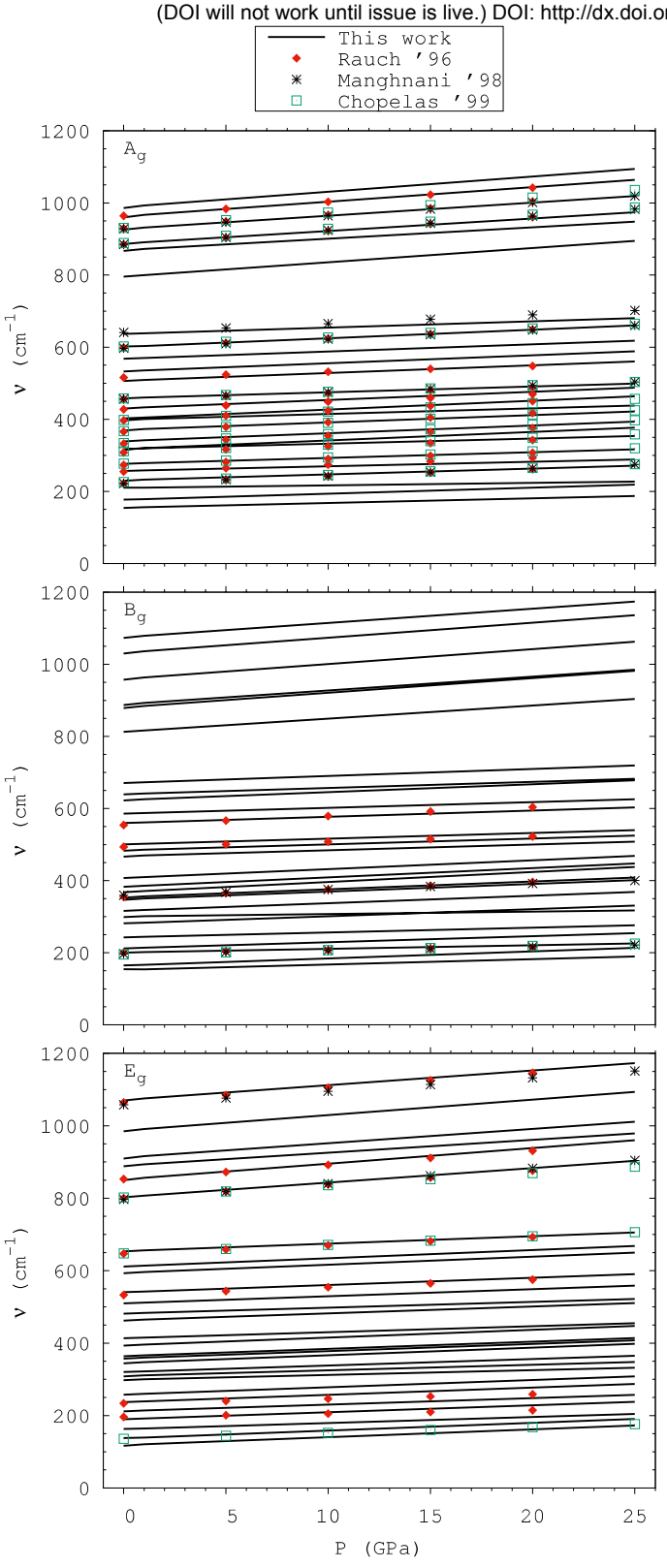

Figure 4 Calculated pressure dependence of Raman frequencies of majorite, as compared with experimental data.

REFERENCES

Akaogi, M., Tanaka, A., and Ito, E. (2002) Garnet–ilmenite–perovskite transitions in the system $Mg_4Si_4O_{12}$–$Mg_3Al_2Si_3O_{12}$ at high pressures and high temperatures: phase equilibria, calorimetry and implications for mantle structure. Physics of the Earth and Planetary Interiors, 132, 303-324.

Aliatis, I., Lambruschi, E., Mantovani, L., Bersani, D., Andò, S., Gatta, G.D., Gentile, P., Salvioli-Mariani, E., Prencipe, M., Tribaudino, M., and Lottici, P.P. (2015) A comparison between ab initio calculated and measured Raman spectrum of triclinic albite ($NaAlSi_3O_8$). Journal of Raman Spectroscopy, 46, 501-508.

Anderson, O.L. (1995) Equations of State of Solids for Geophysics and Ceramic Science. Oxford Monographs on Geology and Geophysics, No. 31. Oxford University Press, New York.

Angel, R.J., Finger, L.W., Hazen, R.M., Kanzaki, M., Weidner, D.J., Leibermann, R.C., and Veblen, D.R. (1989) Structure and twinning of single-crystal $MgSiO_3$ garnet synthesized at 17 GPa and 1800°C. American Mineralogist, 74, 509–512.

Angel, R.J., Mazzucchelli, M.L., Alvaro, M., Nimis, P., and Nestola, F. (2014) Geobarometry from host-inclusion systems: the role of elastic relaxation. American Mineralogist, 99, 2146-2149.

Armbruster, T., Geiger, C.A., and Lager, G.A. (1992) Single-crystal X-ray structure study of synthetic pyrope almandine garnets at 100 K and 293 K. American Mineralogist, 77, 512-521.

Baranek, P., Zicovich-Wilson, C.M., Roetti, C., Orlando, R., and Dovesi, R. (2001) Well localized crystalline orbitals obtained from Bloch functions: the case of $KNbO_3$. Physical Review B, 64, 125102.

Barrow, G.M. (1962). Introduction to Molecular Spectroscopy. McGraw-Hill, New York, 318 pp.

Bass, J.D., and Anderson, D.L. (1984) Composition of the upper mantle: geophysical test of two petrological models. Geophysical Research Letters, 11, 229-232.

Becke, A.D. (1993) Density functional theochemistry. III The role of exact exchange. Journal of Chemical Physics, 98, 5648–5652.

572 Belmonte, D., Ottonello, G., and Vetuschi Zuccolini, M. (2013) Melting of α-Al_2O_3 and
573 vitrification of the undercooled alumina liquid: Ab initio vibrational calculations and their
574 thermodynamic implications. Journal of Chemical Physics, 138, 064507, doi:
575 10.1063/1.4790612.
576 Belmonte, D., Ottonello, G., and Vetuschi Zuccolini, M. (2014) Ab initio thermodynamic and
577 thermophysical properties of sapphirine end-members in the join $Mg_4Al_8Si_2O_{20}$-
578 $Mg_3Al_{10}SiO_{20}$. American Mineralogist, 99, 1449-1461.
579 Broyden, C.G. (1970) The convergence of a class of double-rank minimization algorithms 1.
580 General considerations. Journal of the Institute of Mathematics and its Applications, 6, 76–
581 90.
582 Chaplin, T., Price, G.D., and Ross, N.L. (1998) Computer simulation of the infrared and Raman
583 activity of pyrope garnet, and assignment of calculated modes to specific atomic motions.
584 American Mineralogist, 83, 841–847.
585 Chopelas, A. (1999) Estimates of mantle relevant Clapeyron slopes in the $MgSiO_3$ system from
586 high-pressure spectroscopic data. American Mineralogist, 84, 233–244.
587 Chopelas, A. (2000) Thermal expansivity of mantle relevant magnesium silicates derived from
588 vibrational spectroscopy at high pressure. American Mineralogist, 85, 270–278.
589 Chopelas, A. (2006) Modeling the thermodynamic parameters of six endmember garnets at ambient
590 and high pressures from vibrational data. Physics and Chemistry of Minerals, 33, 363-376.
591 Christensen, U. (1995) Effects of phase transitions on mantle convection. Annual Review of Earth
592 and Planetary Science, 23, 65-87.
593 Civalleri, B., D'Arco, P., Orlando, R., Saunders, V.R., and Dovesi, R. (2001) Hartree-Fock
594 geometry optimization of periodic system with the CRYSTAL code. Chemical Physics
595 Letters, 348, 131–138.
596 Dall'Olio, S., Dovesi, R., and Resta, R. (1997) Spontaneous polarization as a Berry phase of the
597 Hartree-Fock wave function: The case of $KNbO_3$. Physical Review B, 56, 10105–10114.

De La Pierre, M., Orlando, R., Maschio, L., Doll, K., Ugliengo, P., and R. Dovesi (2011) Performance of six functionals (LDA, PBE, PBESOL, B3LYP, PBE0 and WC1LYP) in the simulation of vibrational and dielectric properties of crystalline compounds. The case of forsterite Mg_2SiO_4. Journal of Computational Chemistry, 32, 1775–1784.

De La Pierre, M., Carteret, C., Maschio, L., André, E., Orlando, R., and Dovesi, R. (2014) The Raman spectrum of $CaCO_3$ polymorphs calcite and aragonite: a combined experimental and computational study. Journal of Chemical Physics, 140, 164509.

Demichelis, R., Suto, H., Noël, Y., Sogawa, H., Naoi, T., Koike, C., Chihara, H., Shimobayashi, N., Ferrabone, M., and Dovesi, R. (2012) The infrared spectrum of ortho-enstatite from reflectance experiments and first-principle simulations. Monthly Notices of the Royal Astronomical Society, 420, 147–154.

Deuss, A., Redfern, S.A.T., Chambers, K., and Woodhouse, J.H. (2006) The nature of the 660-kilometer discontinuity in Earth's mantle from global seismic observations of PP precursors. Science, 311, 198-201.

Doll, K. (2001) Implementation of analytical Hartree-Fock gradients for periodic systems. Computer Physics Communications, 137, 74–88.

Doll, K., Harrison, N.M., and Saunders, V.R. (2001) Analytical Hartree-Fock gradients for periodic systems. International Journal of Quantum Chemistry, 82, 1–13.

Dovesi, R., Valenzano, L., Pascale, F., Zicovich-Wilson, C.M., and Orlando, R. (2009) Ab initio quantum-mechanical simulation of the Raman spectrum of grossular. Journal of Raman Spectroscopy, 40, 416–418.

Dovesi, R., De La Pierre, M., Ferrari, A.M., Pascale, F., Maschio, L., and Zicovich-Wilson, C.M. (2011) The IR vibrational properties of six members of the garnet family: a quantum mechanical ab initio study. American Mineralogist, 96, 1787–1798.

Dovesi, R., Saunders, V.R., Roetti, C., Orlando, R., Zicovich-Wilson, C.M., Pascale, F., Civalleri, B., Doll, K., Harrison, N.M., Bush, I.J., D'Arco, Ph., Llunell, M., Causà, M., and Noël, Y.

(2014a) CRYSTAL14 User's Manual. Università di Torino, Torino, 382 pp.

Dovesi, R., Orlando, R., Erba, A., Zicovich-Wilson, C.M., Civalleri, B., Casassa, S., Maschio, L., Ferrabone, M., De La Pierre, M., D'Arco, Ph., Noël, Y., Causà, M., Rérat, M., and Kirtman, B. (2014b) CRYSTAL14: a Program for the ab initio investigation of crystalline solids. International Journal of Quantum Chemistry, 114, 1287–1317.

Erba, A. (2014) On combining pressure and temperature effects on structural properties of crystals with standard ab initio techniques. Journal of Chemical Physics, 141, 124115.

Erba, A., Mahmoud, A., Belmonte, D., and Dovesi, R. (2014) High pressure elastic properties of minerals from ab initio simulations: the case of pyrope, grossular and andradite silicate garnets. Journal of Chemical Physics, 140, 124703, doi: 10.1063/1.4869144.

Erba, A., Navarrete-López, A.M., Lacivita, V., D'Arco, P., and Zicovich-Wilson, C.M. (2015) Katoite under pressure: an ab initio investigation of its structural, elastic and vibrational properties sheds light on the phase transition. Physical Chemistry Chemical Physics, 17, 2660-2669.

Fabrichnaya, O.B., Saxena, S.K., Richet, P., and Westrum, E.F. (2004) Thermodynamic Data, Models, and Phase Diagrams in Multicomponent Oxide Systems. Springer, Berlin-Heidelberg-New York.

Ferrari, A.M., Valenzano, L., Meyer, A., Orlando, R., and Dovesi, R. (2009) Quantum-mechanical ab initio simulation of the Raman and IR spectra of $Fe_3Al_2Si_3O_{12}$ almandine. Journal of Physical Chemistry A, 113, 11289–11294.

Ferraro, J.R., and Ziomek, J.S. (1975) Introductory Group Theory and Its Applications to Molecular Structure. 2nd Edition, Plenum Press, New York, pp. 235-248.

Fletcher, R. (1970) A new approach to variable metric algorithms. Computer Journal, 13, 317–322.

Goldfarb, D. (1970) A family of variable-metric methods derived by variational means. Mathematical Computation, 24, 23–26.

Harte, B. (2010) Diamond formation in the deep mantle: the record of mineral inclusions and their

distribution in relation to mantle dehydration zones. Mineralogical Magazine, 74, 189-215.

Hatch, D.M., and Ghose, S. (1989) Symmetry analysis of the phase transition and twinning in $MgSiO_3$ garnet: implications to mantle mineralogy. American Mineralogist, 74, 1221-1224.

Hernández, E.R., Brodholt, J., and Alfè, D. (2015) Structural, vibrational and thermodynamic properties of Mg_2SiO_4 and $MgSiO_3$ minerals from first-principles simulations. Physics of the Earth and Planetary Interiors, 240, 1-24.

Hess, B.A., Schaad, L.J., Carsky, P., and Zahradnik, R. (1986) Ab initio calculations of vibrational spectra and their use in the identification of unusual molecules. Chemical Reviews, 86, 709–730.

Hirose, K. (2002) Phase transitions in pyrolitic mantle around 670-km depth: implications for upwelling of plumes from the lower mantle. Journal of Geophysical Research: Solid Earth, 107, 2078, doi:10.1029/2001JB000597.

Hirose, K., Fei, Y., Ono, S., Yagi, T., and Funakoshi, K. (2001) In situ measurements of the phase transition boundary in $Mg_3Al_2Si_3O_{12}$: implications for the nature of the seismic discontinuities in the Earth's mantle. Earth and Planetary Science Letters, 184, 567-573.

Hofmeister, A.M., and Chopelas, A. (1991) Vibrational spectroscopy of end-member silicate garnets. Physics and Chemistry of Minerals, 17, 503–526.

Hofmeister, A.M., Fagan, T.J., Campbell, K.M., and Schaal, R.B. (1996) Single-crystal IR spectroscopy of pyrope-almandine garnets with minor amounts of Mn and Ca. American Mineralogist, 81, 418–428.

Hofmeister, A.M., Geisting, P.A., Wopenka, B., Gwanmesia, G.D., and Jolliff, B.L. (2004) Vibrational spectroscopy of pyrope-majorite garnets: structural implications. American Mineralogist, 89, 132–146.

Izraeli, E.S., Harris, J.W., and Navon, O. (1999) Raman barometry of diamond formation. Earth and Planetary Science Letters, 173, 351-360.

Jacobs, M.H.G., and de Jong, B.H.W.S. (2007) Placing constraints on phase equilibria and

thermophysical properties in the system $MgO–SiO_2$ by a thermodynamically consistent vibrational method. Geochimica et Cosmochimica Acta, 71, 3630-3655.

Kato, T., and Kumazawa, M. (1985) Garnet phase of $MgSiO_3$ filling the pyroxene-ilmenite gap at very high temperature. Nature, 316, 803–805.

Kolesov, B.A., and Geiger, C.A. (1998) Raman spectra of silicate garnets. Physics and Chemistry of Minerals, 25, 142–151.

Kolesov, B.A., and Geiger, C.A. (2000) Low-temperature single-crystal Raman spectrum of pyrope. Physics and Chemistry of Minerals, 27, 645–649.

Lee, C., Yang, W., and Parr, R.G. (1988) Development of the Colle-Salvetti correlation-energy formula into a functional of the electron density. Physical Review B, 37, 785–789.

Lu, Y., Yang, Y., and Zhang, P. (2012) Thermodynamic properties and structural stability of thorium dioxide. Journal of Physics: Condensed Matter, 24, 225801.

Manghnani, M.H., Vijayakumar, V., and Bass, J.D. (1998) High-pressure Raman scattering study of majorite-garnet solid solutions in the system $Mg_4Si_4O_{12}$-$Mg_3Al_2Si_3O_{12}$. Pp. 129-138 in: Properties of Earth and Planetary Materials at High Pressure and Temperature (M.H. Manghnani and T. Yagi, editors). Geophysical Monograph No. 101, American Geophysical Union, Washington DC.

Maschio, L., Kirtman, B., Salustro, S., Zicovich-Wilson, C.M., Orlando, R., and Dovesi, R. (2013a) Raman spectrum of pyrope garnet. A quantum mechanical simulation of frequencies, intensities, and isotope shifts. Journal of Physical Chemistry A, 117, 11464–11471.

Maschio, L., Kirtman, B., Rérat, M., Orlando, R., and Dovesi, R. (2013b) Ab initio analytical Raman intensities for periodic systems through a coupled perturbed Hartree-Fock/Kohn-Sham method in an atomic orbital basis. I. Theory. Journal of Chemical Physics, 139, 164101.

Maschio, L., Kirtman, B., Rérat, M., Orlando, R., and Dovesi, R. (2013c) Ab initio analytical Raman intensities for periodic systems through a coupled perturbed Hartree-Fock/Kohn-Sham method in an atomic orbital basis. II. Validation and comparison with experiments. Journal of

Chemical Physics, 139, 164102.

Maschio, L., Demichelis, R., Orlando, R., De La Pierre, M., Mahmoud, A., and Dovesi, R. (2014) The Raman spectrum of grossular garnet: a quantum mechanical simulation of wavenumbers and intensities. Journal of Raman Spectroscopy, 45, 710–715.

McMillan, P., Akaogi, M., Ohtani, E., Williams, Q., Nieman, R., and Sato, R. (1989) Cation disorder in garnets along the $Mg_3Al_2Si_3O_{12}$ – $Mg_4Si_4O_{12}$ join: an Infrared, Raman and NMR Study. Physics and Chemistry of Minerals, 16, 428–435.

Nestola, F., Nimis, P., Ziberna, L., Longo, M., Marzoli, A., Harris, J.W., Manghnani, M.H., and Fedortchouk, Y. (2011) First crystal-structure determination of olivine in diamond: composition and implications for provenance in the Earth's mantle. Earth and Planetary Science Letters, 305, 249-255.

Nestola, F., Merli, M., Nimis, P., Parisatto, M., Kopylova, M., De Stefano, A., Longo, M., Ziberna, L., and Manghnani, M. (2012) In-situ analysis of garnet inclusion in diamond using single-crystal X-ray diffraction and X-ray micro-tomography. European Journal of Mineralogy, 24, 599-606.

Noël, Y., Zicovich-Wilson, C.M., Civalleri, B., D'Arco, Ph., and Dovesi, R. (2002) Polarization properties of ZnO and BeO: an ab initio study through the Berry phase and Wannier functions approaches. Physical Review B, 65, 014111.

Noël, Y., De La Pierre, M., Maschio, L., Rérat, M., Zicovich-Wilson, C.M., and Dovesi, R. (2012) Electronic structure, dielectric properties and infrared vibrational spectrum of fayalite: an ab Initio simulation with an all-electron Gaussian basis set and the B3LYP functional. International Journal of Quantum Chemistry, 112, 2098–2108.

Orlando, R., Torres, F.J., Pascale, F., Ugliengo, P., Zicovich-Wilson, C.M., and Dovesi, R. (2006) Vibrational spectrum of katoite $Ca_3Al_2[(OH)_4]_3$: a periodic ab initio study. Journal of Physical Chemistry B, 110, 692–701.

Ottonello, G., Civalleri, B., Ganguly, J., Vetuschi Zuccolini, M., and Noël, Y. (2009)

Thermophysical properties of the α-β-γ polymorphs of Mg_2SiO_4: a computational study. Physics and Chemistry of Minerals, 36, 87-106.

Ottonello, G., Civalleri, B., Ganguly, J., Perger, W.F., Belmonte, D., and Vetuschi Zuccolini, M. (2010a) Thermo-chemical and thermo-physical properties of the high-pressure phase anhydrous B ($Mg_{14}Si_5O_{24}$): An ab-initio all-electron investigation. American Mineralogist, 95, 563-573.

Ottonello, G., Vetuschi Zuccolini, M., and Belmonte, D. (2010b). The vibrational behaviour of silica clusters at the glass transition: Ab initio calculations and thermodynamic implications. Journal of Chemical Physics, 133, 104508, doi: 10.1063/1.3483195.

Ottonello, G., Attene, M., Ameglio, D., Belmonte, D., Vetuschi Zuccolini, M., and Natali, M. (2013) Thermodynamic investigation of the CaO-Al_2O_3-SiO_2 system at high P and T through polymer chemistry and convex-hull techniques. Chemical Geology, 346, 81-92.

Pascale, F., Zicovich-Wilson, C.M., López Gejo, F., Civalleri, B., Orlando, R., and Dovesi, R. (2004) The calculation of the vibrational frequencies of crystalline compounds and its implementation in the crystal code. Journal of Computational Chemistry, 25, 888–897.

Pascale, F., Catti, M., Damin, A., Orlando, R., Saunders, V.R., and Dovesi, R. (2005a) Vibration frequencies of $Ca_3Fe_2Si_3O_{12}$ andradite. An ab initio study with the CRYSTAL code. Journal of Physical Chemistry B, 109, 18522–18527.

Pascale, F., Zicovich-Wilson, C.M., Orlando, R., Roetti, C., Ugliengo, P., and Dovesi, R. (2005b) Vibration frequencies of $Mg_3Al_2Si_3O_{12}$ pyrope. An ab initio study with the CRYSTAL code. Journal of Physical Chemistry B, 109, 6146–6152.

Pavese, A., Artioli, G., and Prencipe, M. (1995) X-ray single-crystal diffraction study of pyrope in the temperature range 30-973 K. American Mineralogist, 80, 457−464.

Pigott, J.S., Wright, K., Gale, J.D., and Panero, W.R. (2015) Calculation of the energetics of water incorporation in majorite garnet. American Mineralogist, 100, 1065-1075.

Prencipe, M., Pascale, F., Zicovich-Wilson, C.M., Saunders, V.R., Orlando, R., and Dovesi, R.

(2004) The vibrational spectrum of calcite ($CaCO_3$): an ab initio quantum mechanical calculation. Physics and Chemistry of Minerals, 31, 559–564.

Prencipe, M., Scanavino, I., Nestola, F., Merlini, M., Civalleri, B., Bruno, M., and Dovesi, R. (2011) High-pressure thermo-elastic properties of beryl ($Al_4Be_6Si_{12}O_{36}$) from ab initio calculations, and observations about the source of thermal expansion. Physics and Chemistry of Minerals, 38, 223-239.

Prencipe, M., Maschio, L., Kirtman, B., Salustro, S., Erba, A., and Dovesi, R. (2014) Raman spectrum of $NaAlSi_2O_6$ jadeite. A quantum mechanical simulation. Journal of Raman Spectroscopy, 45, 703–709.

Rauch, M., Keppler, H., Häfner, W., Poe, B., and Wokaun, A. (1996) A pressure-induced phase transition in $MgSiO_3$-rich garnet revealed by Raman spectroscopy. American Mineralogist, 81, 1289–1292.

Ringwood, A.E. (1991) Phase transformations and their bearing on the constitution and dynamics of the mantle. Geochimica et Cosmochimica Acta, 55, 2083-2110.

Saikia, A., Frost, D.J., and Rubie, D.C. (2008) Splitting of the 520-kilometer seismic discontinuity and chemical heterogeneity in the mantle. Science, 319, 1515-1518.

Schmeling, H., Marquart, G., and Ruedas, T. (2003) Pressure- and temperature-dependent thermal expansivity and the effect on mantle convection and surface observables. Geophysical Journal International, 154, 224-229.

Shanno, D.F. (1970) Conditioning of quasi-Newton methods for function minimization. Mathematical Computation, 24, 647–656.

Stephens, P.J., Devlin, F.J., Chabalowski, C.F., and Frisch, M.J. (1994) Ab initio calculation of vibrational absorption and circular dichroism spectra using density functional force fields. Journal of Physical Chemistry, 98, 11623–11627.

Tosi, N., Yuen, D.A., de Koker, N., and Wentzcovitch, R.M. (2013) Mantle dynamics with pressure- and temperature-dependent thermal expansivity and conductivity. Physics of the

780 Earth and Planetary Interiors, 217, 48-58.

781 Ulian, G., and Valdrè, G. (2015) Density functional investigation of the thermo-physical and
782 thermo-chemical properties of $2M_1$ muscovite. American Mineralogist, 100, 935-944.

783 Ulian, G., Tosoni, S., and Valdrè, G. (2013) Comparison between Gaussian-type orbitals and plane
784 wave ab initio density functional theory modeling of layer silicates: talc $[Mg_3Si_4O_{10}(OH)_2]$ as
785 model system. Journal of Chemical Physics, 139, 204101.

786 Vacher, P., Mocquet, A., and Sotin, C. (1998) Computation of seismic profiles from mineral
787 physics: the importance of the non-olivine components for explaining the 660 km depth
788 discontinuity. Physics of the Earth and Planetary Interiors, 106, 275-298.

789 Valenzano, L., Meyer, A., Demichelis, R., Civalleri, B., and Dovesi, R. (2009) Quantum-
790 mechanical ab-initio simulation of the Raman and IR spectra of $Mn_3Al_2Si_3O_{12}$ spessartine.
791 Physics and Chemistry of Minerals, 36, 415–420.

792 Valenzano, L., Pascale, F., Ferrero, M., and Dovesi, R. (2010) Ab initio quantum-mechanical
793 prediction of the IR and Raman spectra of $Ca_3Cr_2Si_3O_{12}$ uvarovite garnet. International
794 Journal of Quantum Chemistry, 110, 416–421.

795 Vinograd, V.L., Winkler, B., Putnis, A., Kroll, H., Milman, V., Gale, J.D., and Fabrichnaya, O.B.
796 (2006) Thermodynamics of pyrope-majorite, $Mg_3Al_2Si_3O_{12}$-$Mg_4Si_4O_{12}$, solid solution from
797 atomistic model calculations. Molecular Simulation, 32, 85-99.

798 Wang, Y., and Perdew, J.P. (1991) Correlation hole of the spin-polarised electron-gas, with exact
799 small-wave-vector and high-density scaling. Physical Review B, 44, 13298-13307.

800 Wang, Y., Gasparik, T., and Liebermann, R.C. (1993) Modulated microstructure in synthetic
801 majorite. American Mineralogist, 78, 1165-1173.

802 Weidner, D.J., and Wang, Y. (1998) Chemical- and Clapeyron-induced buoyancy at the 660 km
803 discontinuity. Journal of Geophysical Research: Solid Earth, 103, 7431-7441.

804 Winkler, B., Milman, V., Akhmatskaya, E.V., and Nobes, R.H. (2000) Bonding and dynamics of
805 Mg in pyrope: a theoretical investigation. American Mineralogist, 85, 608-612.

Yu, Y.G., Wentzcovitch, R.M., Vinograd, V.L., and Angel, R.J. (2011) Thermodynamic properties of $MgSiO_3$ majorite and phase transitions near 660 km depth in $MgSiO_3$ and Mg_2SiO_4: a first principles study. Journal of Geophysical Research: Solid Earth, 116, B02208.

Zicovich-Wilson, C.M., Pascale, F., Roetti, C., Saunders, V.R., Orlando, R., and Dovesi, R. (2004) The calculation of the vibration frequencies of α-quartz: the effect of hamiltonian and basis set. Journal of Computational Chemistry, 25, 1873–1881.

Zicovich-Wilson, C.M., Torres, F.J., Pascale, F., Valenzano, L., Orlando, R., and Dovesi, R. (2008) Ab initio Simulation of the IR Spectra of Pyrope, Grossular and Andradite. Journal of Computational Chemistry, 29, 2268–2278.